AIAA Aviation Forum and ASCEND co-located Conference Proceedings
29 July - 2 August 2024, Las Vegas, Nevada
AIAA AVIATION FORUM AND ASCEND 2024

10.2514/6.2024-4192

Space-Time Proper Orthogonal Decomposition of Actuation Transients of a Plasma-Controlled Twin-Rectangular Jet

Brandon C. Y. Yeung* and Oliver T. Schmidt†
University of California San Diego, La Jolla, California 92093

The transient dynamics of a turbulent supersonic twin-rectangular jet flow, forced symmetrically at a Strouhal number of 0.9, are investigated using large-eddy simulations (LES). The forcing is provided by localized arc filament plasma actuators (LAFPA), modeled as source terms in the energy equation. Under plasma-actuated control, the statistically stationary jet evolves towards a cyclostationary state over a transient phase. Forcing-induced perturbations of the natural jet are extracted using synchronized simulations of the natural and forced jets. A database is collected that captures an ensemble of realizations of the perturbations within the initial transient. The spatiotemporal dynamics and statistics of the transient are investigated using space-time proper orthogonal decomposition (space-time POD) for each D_2 symmetry component. The eigenvalue spectra unveil low-rank dynamics in the symmetric component. The spatial and temporal structures of the leading modes indicate that the initial pulse of the actuators produces large, impulsive perturbations to the flow field. The symmetric mode reveals the contraction of the shock cells due to the forcing, and shows the evolution of the mean flow deformation transient.

Nomenclature

$\mathcal{A}$	=	linearized Navier-Stokes operator
a	=	space-time POD expansion coefficient
$\boldsymbol{C}$, $\mathbf{C}$	=	two-point correlation tensor
c	=	speed of sound
D_e	=	equivalent nozzle diameter $1.6h$
D_n	=	dihedral group with n mirror symmetries
e	=	spatially-integrated perturbation energy
$\mathcal{F}$	=	Navier-Stokes operator
f	=	frequency
h	=	nozzle height
k	=	actuator temporal signal
L	=	actuator length
l, m	=	actuator spatial supports
M	=	Mach number
$\mathbf{M}$	=	weight matrix
$\mathcal{N}$	=	nonlinear terms in Navier-Stokes equations
$N_{(\cdot)}$	=	number of $(\cdot)$
P	=	actuator power
p	=	pressure
$\boldsymbol{q}$	=	state vector
Re	=	Reynolds number
r	=	radial coordinate
r_0	=	actuator radius
S, $\boldsymbol{s}$	=	energy source
St	=	Strouhal number fD_e/u_j
T	=	temperature
ΔT	=	finite time horizon

*PhD Student, Department of Mechanical and Aerospace Engineering, Student Member AIAA.
†Associate Professor, Department of Mechanical and Aerospace Engineering, Senior Member AIAA.

t	=	time
t_{on}, t_{off}	=	time instants when actuator switches on or off
t_r	=	actuator rise time
u, v, w	=	Cartesian velocity components
$\boldsymbol{W}$	=	weight tensor
$\boldsymbol{x}$	=	spatial location
x, y, z	=	Cartesian coordinates
γ	=	adiabatic constant, c_p/c_V
Λ, λ	=	space-time POD eigenvalues
μ	=	dynamic viscosity
Ω	=	domain of interest
$\boldsymbol{\phi}$, $\boldsymbol{\psi}$, $\boldsymbol{\Phi}$, $\boldsymbol{\Psi}$	=	space-time POD eigenvectors
ρ	=	density
σ	=	actuator sharpness parameter
τ	=	forcing period

Subscript

a	=	acoustic property
j	=	fully-expanded nozzle exit property
n	=	natural jet
t	=	stagnation property
∞	=	ambient property

Superscript

$\tilde{(\cdot)}$	=	estimated ensemble mean
$(\cdot)'$	=	perturbation component

I. Introduction

REDUCING jet noise is one of the key challenges in civil and military aviation. Military-style supersonic jets, in particular, can emit intense noise, the exposure to which jeopardizes the health of personnel working in close proximity. With the advent of modern high-performance computing (HPC), and high-fidelity numerical simulations that take advantage of such resources, the accurate prediction of jet noise is increasingly attainable [1]. Controlling jet noise, however, remains much more challenging. Developing effective control strategies that achieve robust noise reduction requires fundamental insights into the coherent structures in the jet that are the root cause of noise [2]. While significant inroads have been made into understanding the occurrence of such structures and the underlying hydrodynamic instabilities in high-Reynolds number, axisymmetric jets [3], such progress has so far eluded the analysis of jets from complex nozzle geometries that are typical of military-style aircraft. The focus of this work is the supersonic twin-rectangular jet flow recently investigated by Samimy et al. [4] at Ohio State University (OSU). Their experimental efforts have included the use of localized arc filament plasma actuators (LAFPA, [5, 6]) for control, and have resulted in good control authority on twin-rectangular jet flows. In parallel, we have recently conducted large-eddy simulations (LES) of the same jet [7], with plasma actuation modeled numerically [8]. To discover optimal control laws for a complex nozzle geometry such as this, our long-term goal is to explore the use of episode-based machine learning control (MLC). As a first step towards that goal, in this work we investigate the transient dynamics of the plasma-controlled twin jet. The results will inform our design of the prototypical machine learning episode.

When subjected to exogenous forcing, the twin-rectangular jet evolves from a wide-sense stationary state to a wide-sense cyclostationary state. In between, the jet flow satisfies neither statistical assumption. To study this actuation transient, we leverage the modal decomposition technique called space-time proper orthogonal decomposition (space-time POD, [9]). Space-time POD is the most general form of POD originally proposed by [10]. It extracts structures that are coherent in space and over a finite time horizon, and which optimally represent the second-order statistics. Since space-time POD makes no assumptions about the temporal dynamics, it is well-suited to the analysis of flow phenomena that exhibit non-ergodicity [9, 11], such as a transient. More specialized forms of space-time POD have also been developed. Spectral POD (SPOD, [12–15]) requires the flow to be wide-sense stationary. Analogously, cyclostationary SPOD (CS-SPOD, [16]) requires the flow to be wide-sense cyclostationary. When these more restrictive

conditions are met, the corresponding tools should be exploited. However, the actuation transient meets neither condition; as a consequence, we must use space-time POD.

To better capture the effects of plasma actuation on the unsteady turbulent flow field, we employ the technique of synchronized simulations proposed by Nikitin [17, 18] and independently by Unnikrishnan and Gaitonde [19]. A pair of simulations, with and without actuation, are simultaneously advanced from the same initial condition. At subsequent time steps, the difference between the two solutions was shown to be equivalent to the solution to the perturbation Navier-Stokes equations that govern the difference between the time-varying natural and forced flows. Synchronized simulations have been applied to study pipe and channel flows [17, 18], supersonic jets [19], shock-boundary layer interactions [20], and Couette flows [21]. In this work, we use synchronized simulations to generate an ensemble of realizations of the perturbations, then analyze them with space-time POD.

The remainder of this paper is organized as follows. Sections II.A and II.B recapitulate the methodologies of synchronized simulations and space-time POD, respectively. The setup of the LES is summarized in Section III.A. Section III.B describes the spatial symmetries of the turbulent statistics of the twin jet, and how they are exploited for modal decomposition. The modeling of the plasma actuation is outlined in Section III.C. Results from frequency-time and space-time POD analyses are reported in sections IV.A and IV.B, respectively, and summarized in section V.

II. Spatiotemporal statistics of forced transient flows

A. Synchronized simulations

For a state vector $\boldsymbol{q}_\mathrm{f}(\boldsymbol{x},t)$, the forced compressible Navier-Stokes equations (NSE) can be written in operator form as

$$\frac{\partial}{\partial t}\boldsymbol{q}_\mathrm{f} = \mathcal{F}(\boldsymbol{q}_\mathrm{f}) + \boldsymbol{s}, \tag{1}$$

where $\boldsymbol{s} = \boldsymbol{s}(\boldsymbol{x},t)$ is a source term that models the plasma actuation. For the natural jet flow, denoted $\boldsymbol{q}_\mathrm{n}(\boldsymbol{x},t)$, the source term vanishes, i.e.,

$$\frac{\partial}{\partial t}\boldsymbol{q}_\mathrm{n} = \mathcal{F}(\boldsymbol{q}_\mathrm{n}). \tag{2}$$

To study the effects of actuation on the statistically stationary but unsteady natural jet, we decompose the forced flow,

$$\boldsymbol{q}_\mathrm{f}(\boldsymbol{x},t) = \boldsymbol{q}_\mathrm{n} + \boldsymbol{q}, \tag{3}$$

into the natural flow, $\boldsymbol{q}_\mathrm{n}(\boldsymbol{x},t)$, which is interpreted as an unsteady base state, and the perturbations, $\boldsymbol{q}(\boldsymbol{x},t)$, from that base state. Substituting the decomposition (3) into the forced NSE (1) in perturbation form, then removing the unforced NSE (2) gives the governing equations of the perturbations,

$$\frac{\partial}{\partial t}\boldsymbol{q} = \mathcal{A}(\boldsymbol{q}_\mathrm{n})\boldsymbol{q} + \mathcal{N}(\boldsymbol{q}_\mathrm{n},\boldsymbol{q}) + \boldsymbol{s}, \tag{4}$$

where $\mathcal{A}$ is the linearized Navier-Stokes operator and $\mathcal{N}$ captures the nonlinear terms. In the present study, we retain all linear and nonlinear terms. In practice, the perturbation equation (4) is solved using the synchronized simulations method, in conjunction with equation (2). Specifically, an unforced LES and a forced LES are advanced in parallel from the same initial condition. At each time step, the difference between the two flow states is the solution, $\boldsymbol{q}$. For details on the synchronized simulations technique, we refer the reader to [17–19].

B. Space-time POD

In this section we provide an overview of the space-time POD method [9, 11], focusing on its application to the analysis of flow transients. We seek the set of modes, $\boldsymbol{\phi}(\boldsymbol{x},t)$, that optimally represent the second-order space-time statistics of the transient process, $\boldsymbol{q}(\boldsymbol{x},t)$, over a finite time window, $t \in [t_0, t_0+\Delta T]$. Here, $\boldsymbol{q}$ represents the perturbation in section II.A. As $\boldsymbol{q}$ is already a perturbation quantity, we will not again subtract the mean. But note that mean-flow deformations of the base state caused by the forcing will manifest as a steady component of $\boldsymbol{q}$. In general, $\boldsymbol{q}$ may also be complex. To obtain the modes, we construct the weighted space-time inner product

$$\langle \boldsymbol{q}_1(\boldsymbol{x},t), \boldsymbol{q}_2(\boldsymbol{x},t)\rangle_{\boldsymbol{x},t} = \int_{t_0}^{t_0+\Delta T}\int_\Omega \boldsymbol{q}_2^*(\boldsymbol{x},t)\boldsymbol{W}(\boldsymbol{x},t)\boldsymbol{q}_1(\boldsymbol{x},t)\,\mathrm{d}\boldsymbol{x}\,\mathrm{d}t\,, \tag{5}$$

where, Ω is the domain of interest, $(\cdot)^*$ denotes the conjugate transpose, and $\boldsymbol{W}(\boldsymbol{x},t)$ is a Hermitian positive definite weight tensor. The modes, $\boldsymbol{\phi}(\boldsymbol{x},t)$, maximize the projection

$$\lambda = \frac{E\left\{|\left\langle \boldsymbol{q}(\boldsymbol{x},t),\boldsymbol{\phi}(\boldsymbol{x},t)\right\rangle_{\boldsymbol{x},t}|^2\right\}}{\left\langle \boldsymbol{\phi}(\boldsymbol{x},t),\boldsymbol{\phi}(\boldsymbol{x},t)\right\rangle_{\boldsymbol{x},t}}. \tag{6}$$

As equation (6) is the same quantity that is maximized by all variants of space-time POD [9, 11], including SPOD [14, 15] and CS-SPOD [16], the solutions, λ_j and $\boldsymbol{\phi}_j$, are given by the standard weighted Fredholm eigenvalue problem

$$\int_{t_0}^{t_0+\Delta T}\int_{\Omega} \boldsymbol{C}(\boldsymbol{x},\boldsymbol{x}',t,t')\boldsymbol{W}(\boldsymbol{x}',t')\boldsymbol{\phi}(\boldsymbol{x}',t')\,\mathrm{d}\boldsymbol{x}'\,\mathrm{d}t' = \lambda\boldsymbol{\phi}(\boldsymbol{x},t), \tag{7}$$

where $\boldsymbol{C}(\boldsymbol{x},\boldsymbol{x}',t,t') = E\{\boldsymbol{q}(\boldsymbol{x},t)\boldsymbol{q}^*(\boldsymbol{x}',t')\}$ is the two-point space-time correlation tensor. Since $\boldsymbol{q}$ is a fluctuation quantity, the eigenvalue, λ_j, measures the fluctuation energy corresponding to the mode, $\boldsymbol{\phi}_j$, under the norm induced by the space-time inner product in equation (5). Properties analogous to those of more specialized forms of space-time POD also hold for this most general form. Specifically, the modes are mutually orthogonal,

$$\left\langle \boldsymbol{\phi}_j(\boldsymbol{x},t),\boldsymbol{\phi}_k(\boldsymbol{x},t)\right\rangle_{\boldsymbol{x},t} = \delta_{jk}. \tag{8}$$

The modal energies, λ_j, are related to the expansion coefficients, a_j,

$$E\left\{a_j a_k^*\right\} = \lambda_j\delta_{jk}, \tag{9}$$

where $a_j = \left\langle \boldsymbol{q}(\boldsymbol{x},t),\boldsymbol{\phi}_j(\boldsymbol{x},t)\right\rangle_{\boldsymbol{x},t}$. Finally, the modes and their expansion coefficients can be used to reconstruct the transient,

$$\boldsymbol{q}(\boldsymbol{x},t) = \sum_{j=1}^{\infty} a_j\boldsymbol{\phi}_j(\boldsymbol{x},t). \tag{10}$$

Unlike SPOD modes, space-time POD modes, $\boldsymbol{\phi}(\boldsymbol{x},t)$, are time-varying. As such, the latter simultaneously provide both a statistical and a dynamical perspective on the evolution of coherent structures.

To compute space-time POD modes from discretely-sampled and finite data, the correlation tensor must be estimated. By definition, an evolving, transient process is non-ergodic. The statistics must therefore be estimated from an ensemble of realizations of the same (numerical) experiment, rather than from segments of a single long time series as is typically done in SPOD or CS-SPOD. Suppose each of N realizations of the transient consists of N_t snapshots of the flow state, $\mathbf{q}_i^{(k)} \in \mathbb{C}^{N_x}$, with $i = 1,2,\ldots,N_t$, k the realization index, and N_x the number of degrees of freedom. The snapshots are sampled at a time interval of $\Delta t = \Delta T/N_t$. For each realization, we stack the snapshots in a single tall space-time vector,

$$\mathbf{q}^{(k)} = \begin{bmatrix} \mathbf{q}_1^{(k)} \\ \mathbf{q}_2^{(k)} \\ \vdots \\ \mathbf{q}_{N_t}^{(k)} \end{bmatrix} \in \mathbb{C}^{N_xN_t}, \quad k = 1,2,\ldots,N. \tag{11}$$

From the space-time vectors we assemble the data matrix

$$\mathbf{Q} = [\mathbf{q}^{(1)},\mathbf{q}^{(2)},\ldots,\mathbf{q}^{(N)}] \in \mathbb{C}^{N_xN_t\times N}. \tag{12}$$

The two-point space-time correlation tensor is estimated as

$$\mathbf{C} = \frac{1}{N}\mathbf{Q}\mathbf{Q}^*. \tag{13}$$

The weighted eigenvalue decomposition (EVD) of $\mathbf{C}$,

$$\mathbf{C}\mathbf{M}\mathbf{\Phi} = \mathbf{\Phi}\mathbf{\Lambda}, \tag{14}$$

provides the modal energies and modes, which are the nonzero elements of $\mathrm{diag}(\mathbf{\Lambda})$ and the corresponding columns in $\mathbf{\Phi}$, respectively. Here $\mathbf{M}$ is a diagonal positive definite weight matrix that discretizes the space-time inner product in equation (5). In practice, rather than diagonalizing $\mathbf{C}$, we invoke the method-of-snapshots [22] and obtain the same modes and nonzero modal energies from the much smaller EVD,

$$\frac{1}{N}\mathbf{Q}^*\mathbf{M}\mathbf{Q}\mathbf{\Psi} = \mathbf{\Psi}\mathbf{\Lambda}, \quad \text{with} \quad \mathbf{\Phi} = \frac{1}{\sqrt{N}}\mathbf{Q}\mathbf{\Psi}\mathbf{\Lambda}^{-\frac{1}{2}}. \tag{15}$$

Table 1 Parameters of the synchronized simulations, shared between the natural and forced jets.

M_j	M_a	Re_j	p_t/p_∞	p_j/p_∞	T_t/T_∞	T_j/T_∞	N_{cv}	$\mathrm{d}tu_j/h$
1.5	1.25	1.07×10^6	3.671	1	1	0.69	77.0×10^6	0.00125

III. Twin-rectangular jet flow

A. Numerical setup

The parameters of the LES closely follow the setup in our previous study of the forced supersonic twin-rectangular jet [8]. The simulations were carried out using the unstructured compressible solver 'Charles' by Cadence [23]. The jet has a Mach number of $M_j = u_j/c_j = 1.5$, where u_j and c_j are the streamwise velocity and speed of sound, respectively, on the centerline of the nozzle exit. Its acoustic Mach number is $M_a = u_j/c_\infty$, where c_∞ is the ambient speed of sound. The jet is nominally ideally-expanded, $p_j/p_\infty = 1$, where p is the pressure, but contains shocks due to the biconical nozzle geometry. The nozzle exit temperature is $T_j/T_\infty = 0.69$, i.e., the jet is cold. The Reynolds number is $Re_j = \rho_j u_j D_e/\mu_j = 1.07 \times 10^6$, where ρ is the density, μ is the dynamic viscosity, $D_e = 1.6h$ is the equivalent nozzle diameter, and h is the nozzle height. The nozzle pressure (NPR) and temperature ratios (NTR) are $p_t/p_\infty = 3.671$ and $T_t/T_\infty = 1$, respectively. A wall model is applied to the nozzle interior. The flow state has been non-dimensionalized by the jet exit conditions: density by ρ_j, velocities by u_j, temperature by T_j, and pressure by $\rho_j u_j^2$. Lengths are non-dimensionalized by h, and time by h/u_j. Dimensionless frequencies are expressed in terms of the Strouhal number based on the equivalent nozzle diameter, $St_{D_e} = fD_e/u_j$; for convenience, in the following we will drop the subscript from St. These parameters are shared between the natural and forced simulations, and are summarized in Table 1.

Figure 1(a) shows the full twin-rectangular nozzle geometry, which is explicitly included in the computational grid. The grid is discretized by approximately 77 million cells. A cavity just upstream of the nozzle lips, shown in Fig. 1(b), houses the idealized electrodes. Each pair of electrodes acts as one plasma actuator. Each nozzle includes eight actuators: three on the horizontal upper lip, three on the horizontal lower lip, and two on the vertical outboard lip. Only the six actuators on the upper and lower lips are active in the companion experiments at OSU [4], and this is the case in our LES as well. The LES of the unforced jet has been validated against experiments [6]. In particular, predictions of the overall sound pressure level (OASPL) match experimental measurements to within one dB for most microphone locations. For more details on the numerical setup, including its validation, we refer the reader to [6–8, 24].

To obtain multiple independent realizations for space-time POD, snapshots of the statistically stationary, natural jet are sampled from a previous simulation [7] and used as initial conditions for the transient simulations. Due to the present need to capture the intense disturbances created by the actuators, the grid used in the synchronized simulations has undergone slight refinement around the nozzle lip compared to the previous stationary simulation. The grid mismatch between the pre-existing and current computations causes a grid transient to appear in both synchronized simulations (natural and forced). In the perturbation, $\boldsymbol{q}$, however, we expect the effect to be minimal. Based on estimates of the two-time autocorrelation, the initial conditions are spaced $(\Delta t)_{\mathrm{IC}} = 100$ apart in time to guarantee their statistical independence. For simplicity and consistency, we set the length of the time window for space-time POD to be the same, $\Delta T = 100$.

For this study, $N = 17$ realizations of the transient were obtained for statistical analysis. Snapshots of the five primitive variables, ρ, u, v, w, and T, are extracted from the LES at intervals of $\Delta tu_j/h = 0.25$, then interpolated from the unstructured grid onto a Cartesian grid. The variables are assembled in the state vector $\boldsymbol{q} = [\rho, u, v, w, T]^{\mathrm{T}}$. Since the flow is compressible, we use the weight tensor

$$\boldsymbol{W}(\boldsymbol{x},t) = \mathrm{diag}\left(\left[\frac{\tilde{T}(\boldsymbol{x},t)}{\gamma\tilde{\rho}(\boldsymbol{x},t)M_j^2}, \tilde{\rho}(\boldsymbol{x},t), \tilde{\rho}(\boldsymbol{x},t), \tilde{\rho}(\boldsymbol{x},t), \frac{\tilde{\rho}(\boldsymbol{x},t)}{\gamma(\gamma-1)\tilde{T}(\boldsymbol{x},t)M_j^2}\right]\right), \tag{16}$$

where γ is the adiabatic constant. The inner product in equation (5) thus induces the compressible energy norm [25]. The $\tilde{(\cdot)}$ notation refers to the estimated ensemble mean,

$$\tilde{\boldsymbol{q}}(\boldsymbol{x},t) = \frac{1}{N}\sum_{k=1}^{N} \boldsymbol{q}_{\mathrm{n}}^{(k)}(\boldsymbol{x},t). \tag{17}$$

Here, we have chosen the ensemble mean of the natural jet, since the natural jet is considered the base state in the

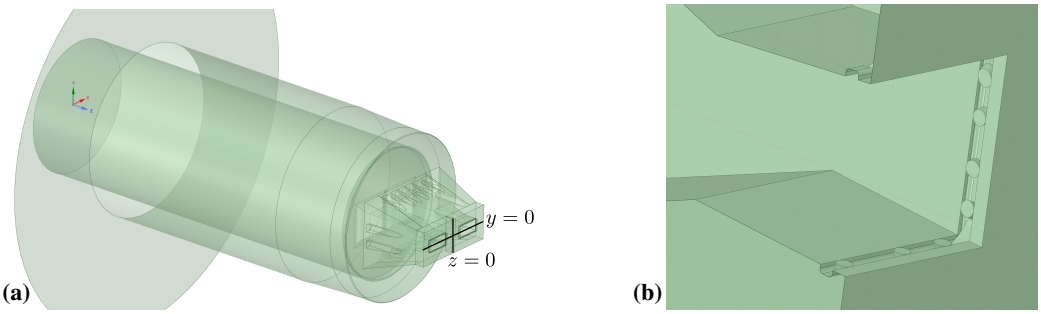

Fig. 1 Nozzle geometry [6]: (a) the supply pipe and the twin-rectangular nozzles; (b) a cutout view of one of the nozzles, showing the idealized electrodes recessed into the cavity near the exit. The axes $y = 0$ and $z = 0$ are the major and minor axes, respectively.

framework of synchronized simulations. To prevent the synchronized natural and forced jet flows from becoming entirely decorrelated due to turbulence, we restrict the spatiotemporal norm in equations (5) and (16) to $t \in [0, 20]$ by setting

$$\boldsymbol{W}(\boldsymbol{x}, t) = 0 \quad \text{for} \quad t > 20. \tag{18}$$

This window, $t \in [0, 20]$, spans approximately 11 actuation periods and focuses on the initial transient.

B. Statistical symmetries

When symmetries are present in a flow, they should be exploited in modal decompositions, including space-time POD. Doing so reduces computational complexity, accelerates statistical convergence, and, perhaps most importantly, improves the interpretability of the results. The twin-rectangular jet nozzles are symmetric about the major and minor axes, $y = 0$ and $z = 0$, respectively. The geometry thus belongs in the dihedral group D_2. In the instantaneous flow, geometrical symmetries are broken by turbulence; however, they are imprinted on the turbulent statistics. Nevertheless, when the statistics are estimated from data, these symmetries will be imperfectly expressed, and must be enforced. In recent studies, we enforced D_2 symmetry on the SPOD analysis of the natural twin-rectangular jet [7] and BMD analysis of the forced jet [8]. Here we extend the framework to space-time POD.

Without loss of generality, the perturbations can be decomposed into four D_2 symmetry components (see e.g. Sirovich and Park [26]),

$$\boldsymbol{q}^{(k)}(x, y, z, t) = \boldsymbol{q}^{(k)}_{\mathrm{SS}}(x, y, z, t) + \boldsymbol{q}^{(k)}_{\mathrm{SA}}(x, y, z, t) + \boldsymbol{q}^{(k)}_{\mathrm{AS}}(x, y, z, t) + \boldsymbol{q}^{(k)}_{\mathrm{AA}}(x, y, z, t), \tag{19}$$

where the first and second letters in the subscripts denote symmetry (S) or antisymmetry (A) about the major and minor axes, respectively. The symmetry components are given by

$$\boldsymbol{q}^{(k)}_{\mathrm{SS}}(x, y, z, t) = \frac{1}{4}\begin{bmatrix} \rho^{(k)}(x, y, z, t) + \rho^{(k)}(x, -y, z, t) + \rho^{(k)}(x, y, -z, t) + \rho^{(k)}(x, -y, -z, t) \\ u^{(k)}(x, y, z, t) + u^{(k)}(x, -y, z, t) + u^{(k)}(x, y, -z, t) + u^{(k)}(x, -y, -z, t) \\ v^{(k)}(x, y, z, t) - v^{(k)}(x, -y, z, t) + v^{(k)}(x, y, -z, t) - v^{(k)}(x, -y, -z, t) \\ w^{(k)}(x, y, z, t) + w^{(k)}(x, -y, z, t) - w^{(k)}(x, y, -z, t) - w^{(k)}(x, -y, -z, t) \\ T^{(k)}(x, y, z, t) + T^{(k)}(x, -y, z, t) + T^{(k)}(x, y, -z, t) + T^{(k)}(x, -y, -z, t) \end{bmatrix}, \tag{20}$$

$$\boldsymbol{q}^{(k)}_{\mathrm{SA}}(x, y, z, t) = \frac{1}{4}\begin{bmatrix} \rho^{(k)}(x, y, z, t) + \rho^{(k)}(x, -y, z, t) - \rho^{(k)}(x, y, -z, t) - \rho^{(k)}(x, -y, -z, t) \\ u^{(k)}(x, y, z, t) + u^{(k)}(x, -y, z, t) - u^{(k)}(x, y, -z, t) - u^{(k)}(x, -y, -z, t) \\ v^{(k)}(x, y, z, t) - v^{(k)}(x, -y, z, t) - v^{(k)}(x, y, -z, t) + v^{(k)}(x, -y, -z, t) \\ w^{(k)}(x, y, z, t) + w^{(k)}(x, -y, z, t) + w^{(k)}(x, y, -z, t) + w^{(k)}(x, -y, -z, t) \\ T^{(k)}(x, y, z, t) + T^{(k)}(x, -y, z, t) - T^{(k)}(x, y, -z, t) - T^{(k)}(x, -y, -z, t) \end{bmatrix}, \tag{21}$$

Table 2 Non-dimensionalized plasma actuation parameters. Ambient temperature and pressure are assumed to be 293 K and 1 atm, respectively.

Case	$P/(\rho_j u_j^3 h^2)$	r_0/h	L/h	σ	$t_{\text{on}}u_j/h$	$t_{\text{off}}u_j/h$	$t_r u_j/h$	St_0
Forced	6.16	0.02	0.29	5	0	0.001875	2.5×10^{-5}	0.9

$$\boldsymbol{q}^{(k)}_{\text{AS}}(x,y,z,t) = \frac{1}{4}\begin{bmatrix} \rho^{(k)}(x,y,z,t) - \rho^{(k)}(x,-y,z,t) + \rho^{(k)}(x,y,-z,t) - \rho^{(k)}(x,-y,-z,t) \\ u^{(k)}(x,y,z,t) - u^{(k)}(x,-y,z,t) + u^{(k)}(x,y,-z,t) - u^{(k)}(x,-y,-z,t) \\ v^{(k)}(x,y,z,t) + v^{(k)}(x,-y,z,t) + v^{(k)}(x,y,-z,t) + v^{(k)}(x,-y,-z,t) \\ w^{(k)}(x,y,z,t) - w^{(k)}(x,-y,z,t) - w^{(k)}(x,y,-z,t) + w^{(k)}(x,-y,-z,t) \\ T^{(k)}(x,y,z,t) - T^{(k)}(x,-y,z,t) + T^{(k)}(x,y,-z,t) - T^{(k)}(x,-y,-z,t) \end{bmatrix}, \tag{22}$$

and

$$\boldsymbol{q}^{(k)}_{\text{AA}}(x,y,z,t) = \frac{1}{4}\begin{bmatrix} \rho^{(k)}(x,y,z,t) - \rho^{(k)}(x,-y,z,t) - \rho^{(k)}(x,y,-z,t) + \rho^{(k)}(x,-y,-z,t) \\ u^{(k)}(x,y,z,t) - u^{(k)}(x,-y,z,t) - u^{(k)}(x,y,-z,t) + u^{(k)}(x,-y,-z,t) \\ v^{(k)}(x,y,z,t) + v^{(k)}(x,-y,z,t) - v^{(k)}(x,y,-z,t) - v^{(k)}(x,-y,-z,t) \\ w^{(k)}(x,y,z,t) - w^{(k)}(x,-y,z,t) + w^{(k)}(x,y,-z,t) - w^{(k)}(x,-y,-z,t) \\ T^{(k)}(x,y,z,t) - T^{(k)}(x,-y,z,t) - T^{(k)}(x,y,-z,t) + T^{(k)}(x,-y,-z,t) \end{bmatrix}. \tag{23}$$

Following common practice, for each component we conduct an independent analysis using space-time POD. That is, we ignore nonlinear interactions between symmetry components [8].

C. Actuation

The numerical modeling of the plasma actuators closely follows our recent work on the forced twin jet [8], which was in turn an adaptation of the actuator model proposed by Kim et al. [27]. For notational simplicity only, in this section we adopt cylindrical coordinates, (r, z), and temporarily align each plasma arc with the axial direction, along the z-axis. Each actuator is modeled as a source term of the energy equation,

$$S(r,z,t) = k(t)l(r)m(z)\frac{P}{\pi r_0^2 L}, \tag{24}$$

where P is an amplitude with dimensions of power. The spatial support of the plasma arc is a smoothed cylinder with radius r_0 and length L. Specifically, the support is defined by the functions

$$l(r) = \frac{1}{2}\left[\tanh\left(-\sigma\left(\frac{r}{r_0} - \frac{1}{2}\right)\right) + 1\right] \tag{25}$$

and

$$m(z) = -\frac{1}{2}\left[\tanh\left(-\sigma\frac{z + L/2}{r_0}\right) + 1\right] + \frac{1}{2}\left[\tanh\left(-\sigma\frac{z - L/2}{r_0}\right) + 1\right], \tag{26}$$

where σ is a sharpness parameter. The temporal support is given by

$$k(t) = \frac{1}{2}\left[\tanh\left(\frac{(t - n\tau) - t_{\text{on}}}{t_r}\right) - \tanh\left(\frac{(t - n\tau) - t_{\text{off}}}{t_r}\right)\right], \quad \text{with} \quad n = \lfloor t/\tau \rfloor. \tag{27}$$

This signal is a smoothed pulse wave with period τ. Within each period, the actuator switches on at time t_{on}, and off at time t_{off}, with a rise time of t_r. The values for these parameters are estimated based on the available experimental measurements, and are displayed in Table 2. The duty cycle, $(t_{\text{off}} - t_{\text{on}})/\tau \approx 0.1\%$, is short. As a result, the actuation approximates an impulse train or Dirac comb, which is a periodic but non-harmonic forcing. All harmonics of the actuation frequency, St_0, are thus forced simultaneously.

To maximize control authority, the actuation must be consistent with the inherent symmetries of the flow, in this case D_2 symmetry. In the unforced case, the twin-rectangular jet is known to emit screech tones in the AS and AA symmetry

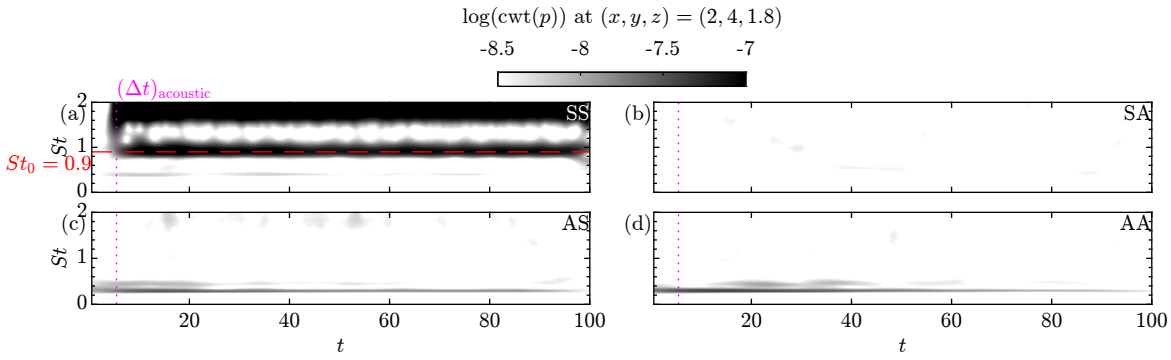

Fig. 2 Ensemble-averaged continuous wavelet transform of the pointwise pressure, $p(x = 2, y = 4, z = 1.8, t)$, in the forced jet. Morse wavelets were used. The SS forcing frequency, St_0, is marked by the red dashed line. The acoustic time-of-flight from the nozzle centerline to the probe location is marked by the magenta dotted line.

components [7]. For this work, we fire all actuators in-phase with each other, corresponding to the SS symmetry. The dynamics of the leading space-time POD modes of each symmetry will lend insight into the evolution of the jet flow from its preferred symmetries, AS and AA, to the forced symmetry, SS. In their experiments, [4] demonstrated significant reduction in twin-rectangular jet noise using a forcing frequency of $St_0 = 0.9$. We therefore adopt the same forcing frequency.

IV. Transient dynamics and statistics

A. Frequency-time analysis

Before conducting a global analysis using space-time POD, we first quantify the transient dynamics of the forced jet from a local perspective. We extract the pressure signal from a probe location in the freestream, $(x, y, z) = (2, 4, 1.8)$, to focus on acoustic disturbances. Figure 2 reports the frequency-time diagrams of the pressure signal, computed using the continuous wavelet transform. The acoustic time-of-flight, $(\Delta t)_{\text{acoustic}}$, from the nozzle centerline at $(x, y, z) = (0, 0, 1.8)$ to the probe is estimated from the jet speed of sound, $c_j = \sqrt{\gamma p_\infty / \rho_j}$, which, for a cold jet, is slower than the ambient speed of sound, c_∞. Figure 2(a) shows the forced SS component becoming active simultaneously at the fundamental and first harmonic frequencies, St_0 and $2St_0$, as the acoustic signal from the first actuation cycle reaches the probe after a time delay of $(\Delta t)_{\text{acoustic}}$. A much weaker peak is also visible at $St = 0.4$. This peak is intermittent, and appears unaffected by the forcing. The remaining symmetries, however, are not energized at St_0 or its harmonics. The SA symmetry in figure 2(b) shows no significant activity whatsoever. The AS and AA symmetries in figure 2(c,d) display a screech tone at $St = 0.3$. The screech is present in the natural jet, and appears largely unaffected by the arrival of the first actuation signal at $t = (\Delta t)_{\text{acoustic}}$, nor by the subsequent actuation cycles. An exception is a gradual but slight reduction in the screech amplitude from $t = 0$ to $t = 100$. The frequency-time analysis thus provides the first indication that periodic forcing of the SS symmetry at $St = 0.9$ does not effectively mitigate screech.

B. Space-time POD energy and modes

The space-time POD mode energies of each of the four D_2 symmetry components are shown in figure 3. It is immediately apparent that the leading SS mode is extremely energetic. It represents $\lambda_1 / \sum_j \lambda_j = 41\%$ of the total energy in the SS component. For comparison, the leading mode in the SA, AS, and AA components each accounts for just 7–8% of the total energy in the respective symmetry. The large separation between the leading and suboptimal eigenvalues in SS indicates low-rank behavior, which is commonly observed in SPOD and interpreted as a sign of dominant hydrodynamic instabilities or other physical mechanisms [3]. In this case, the rank separation in SS corresponds to the large perturbations to the natural flow that are directly linked to the SS forcing.

The SA, AS, and AA leading eigenvalues are all an order-of-magnitude less energetic than the SS leading mode. To study the differences between these low-energy modes, the inset in figure 3 zooms in on the first five eigenvalues for each symmetry, in the region $\lambda_j \in [1.25, 2]$. Excluding the SS symmetry, the AS leading mode has the most energy. Among all four symmetries, the AS modes also display the fastest rank decay as the mode number, j, increases.

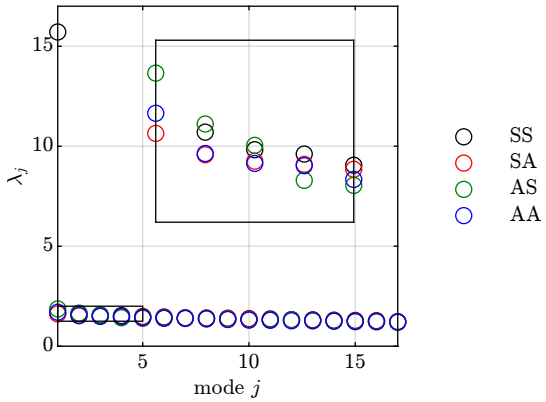

Fig. 3 Space-time POD mode energy for each symmetry component. The inset zooms in on the leading five modes.

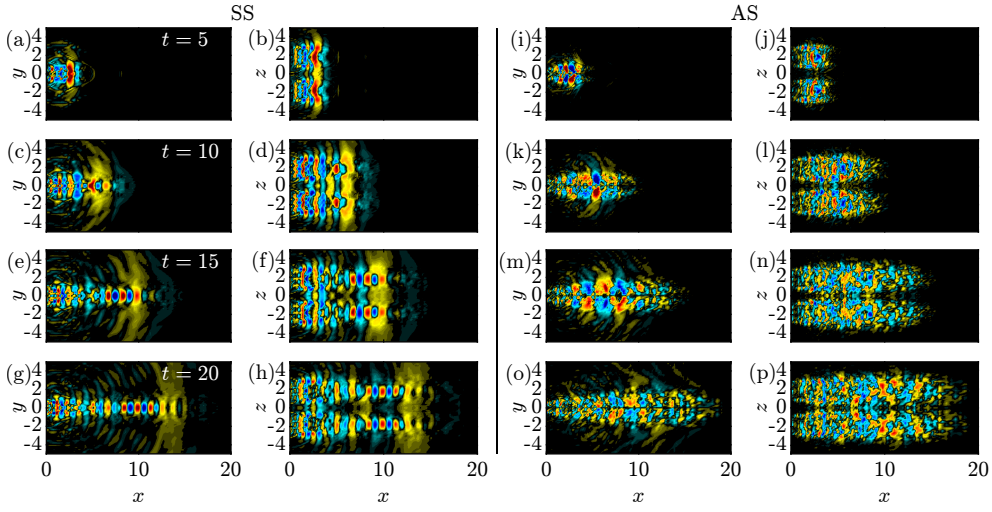

Fig. 4 Pressure component of leading space-time POD mode: (a–h) SS; (i–p) AS symmetry components, visualized at $t = 5$ (a,b,i,j), 10 (c,d,k,l), 15 (e,f,m,n), and 20 (g,h,o,p), on the $z = 1.8$ (a,c,e,g,i,k,m,o) and $y = 0.25$ (b,d,f,h,j,l,n,p) planes.

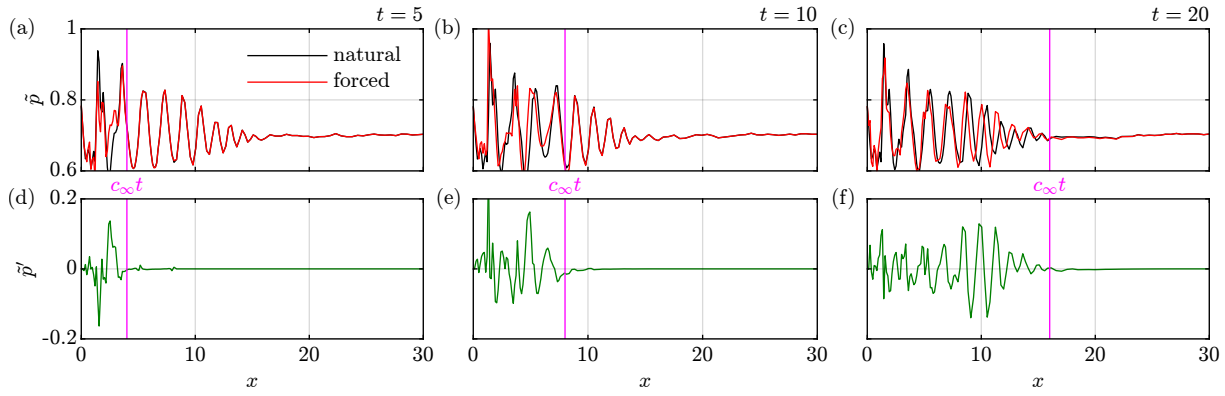

Fig. 5 Pressure along the nozzle centerline, $y = 0$ and $z = 1.8$, for the SS component: (a–c) ensemble mean of the natural and forced transients; (d–f) difference between the respective ensemble mean. Three time instances are displayed: $t = 5$ (a,d), 10 (b,e), and 20 (c,f). The estimated location of the initial acoustic wave, $x = c_\infty t$, is marked by the magenta line.

Figure 4 displays the pressure component of the leading space-time POD mode for the SS and AS symmetry components, at four representative time instances: $t = 5, 10, 15, 20$. The pressure component is reconstructed using the linearized ideal gas equation of state,

$$\phi_p = \tilde{\rho}\phi_T + \phi_\rho \tilde{T}, \tag{28}$$

where ϕ_ρ and ϕ_T are the density and temperature components, respectively, of the mode ϕ, and $\tilde{(\cdot)}$ represents the ensemble mean of the natural jet. For the SS symmetry in figure 4(a–h), we observe an acoustic wave front that is created by the initial pulse of the actuator, corresponding to the response of the natural jet to the impulsive forcing. This wave front propagates downstream at the speed of sound. Subsequent actuation cycles also generate aft-angle acoustic waves at the forcing frequency, St_0, but with significantly lower amplitudes than the impulse response.

Behind the impulsive wave front, in the downstream region $x \gtrsim 5$, modes are visible along the centerline of each jet. Close examination of the four time instances reveals that the nodes and antinodes of these modes are stationary in space. These modes are not hydrodynamic in origin. Instead, they result from forcing-induced deformations of the mean flow, specifically the shock cell structure. Figure 5 compares the ensemble mean of the transients of the natural and forced jets, as well as their difference, along the centerline of one nozzle, at $y = 0$ and $z = 1.8$, for the SS symmetry component. Also shown is the location of the initial acoustic wave front, estimated from the ambient speed of sound, c_∞. The acoustic wave clearly demarcates the region as yet unaffected by the forcing, $x > c_\infty t$, from the region that has felt its influence, $x < c_\infty t$. For $x > c_\infty t$, the natural and forced mean flows overlap. For $x < c_\infty t$, the two deviate from each other. In particular, the forcing causes the shock cells to shift further upstream, perhaps entailing a slight contraction of the potential core length. The steady phase difference between the shocks of the natural and forced jets explains the wave-like pattern along the centerline of the SS space-time POD mode.

Returning to the POD modes in figure 4(i–p), the AS symmetry component, which is known to manifest jet screech in the natural twin-rectangular jet [7], does not exhibit the upstream-propagating hydrodynamic and acoustic waves that are required to close the screech feedback loop [28]. This indicates the screech feedback mechanism is present in both jets. Moreover, the waves involved in screech in both jets remain in phase with each other, so that they vanish in the perturbation, i.e., the difference between the two transients. It is thus unlikely that the present actuation strategy can achieve significant screech mitigation. This finding is consistent with the frequency-time analysis in figure 2.

Rather, the main effect of the forcing on the AS component is the impulse response from the initial actuation cycle. In contrast to the SS mode in figure 4(a,b), small-scale turbulent structures are generated almost instantaneously in the AS mode in 4(i,j). Superimposed on the background turbulence is a dispersive wavepacket that emerges in 4(i,j), then increases its wavelength from 4(i,j) through 4(n), before disappearing in 4(o,p). Subsequent actuation cycles do not create such a wavepacket.

In figure 6, we examine the instantaneous, spatially-integrated energy of the SS and AS leading modes, given by

$$e_1(t) = \lambda_1 \|\boldsymbol{\phi}_1(\boldsymbol{x}, t)\|_{\boldsymbol{x}}^2 = \lambda_1 \int_\Omega \boldsymbol{\phi}_1^*(\boldsymbol{x}, t) \boldsymbol{W}(\boldsymbol{x}, t) \boldsymbol{\phi}_1(\boldsymbol{x}, t)\, \mathrm{d}\boldsymbol{x}\,. \tag{29}$$

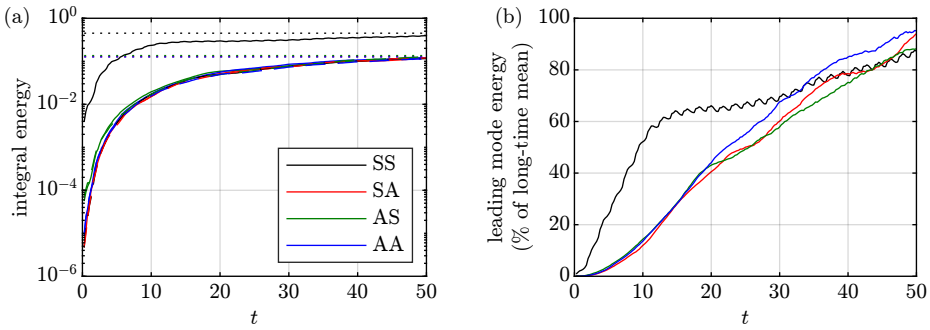

Fig. 6 Spatially-integrated instantaneous energy: (a) mode 1 (solid lines), mode 2 (dashed lines), and time-averaged energy of mode 1 as $t \to \infty$ (dotted lines); (b) instantaneous energy of mode 1 as a percentage of the time-averaged energy.

We point out that the modes are normalized only in the full spatiotemporal norm, $\langle \cdot, \cdot \rangle_{\boldsymbol{x},t}$, not the spatial norm, $\langle \cdot, \cdot \rangle_{\boldsymbol{x}}$. In addition, despite setting $\boldsymbol{W}(\boldsymbol{x}, t > 20) = 0$ in the space-time POD calculation, the modes have finite temporal support for $t > 20$. This is due to the use of method-of-snapshots, as shown in equation (15). To recover the instantaneous energy of the mode beyond $t = 20$, we use the compressible energy weight displayed in equation (16), without restricting it in time. For visual clarity only, in figure 6 we focus on the time window $t \in [0, 50]$. In 6(a), the instantaneous perturbation energy represented by the leading mode is highest for the SS symmetry component, followed by the AS component. This is consistent with the eigenvalue spectra in figure 3. For the AS symmetry, the instantaneous energy of the leading mode dips below that of the second mode during $1 \lesssim t \lesssim 3$, and again during $35 \lesssim t \lesssim 80$. Such mode-switching behavior is permitted because the space-time POD modes are energetically optimal (in a spatiotemporal-integral sense) only for $t \leq 20$. The dotted lines mark the time-averaged spatially-integrated energy of the leading mode of each symmetry component after the forced jet has reached statistical cyclostationarity. Clearly, the instantaneous energy approaches the average energy at large t.

To quantify the rate at which each symmetry approaches cyclostationarity, figure 6(b) reports the instantaneous energy during the transient as a percentage of the average energy in the cyclostationary state. As expected from the SS forcing, the percentage energy of the SS leading mode rises rapidly in the initial transient, $t \lesssim 10$. The rate of increase of the SS mode is also higher than that of the other symmetries, since the forcing directly energizes the SS component, but can only contribute to the remaining components through nonlinear cross-symmetry interactions [8]. The percentage energy curve of the SS mode displays a wavy pattern due to the periodic forcing. Beyond $t = 10$, however, the rate of increase of the SS mode energy slows significantly, allowing the other symmetries to gradually catch up. As a result, all four symmetries manage to capture approximately 90% of the cyclostationary energy at $t \approx 50$. In short, from an energetic view, the actuation transient can be considered largely over by $t \approx 50$, at which point time-averaged statistics, e.g. far-field acoustics, may begin to be collected.

V. Summary

When a statistically stationary turbulent flow is subjected to periodic forcing, it first undergoes a transient state before eventually attaining statistical cyclostationarity. During its transient phase, the statistics of the flow are time-varying and aperiodic. Consequently, the modal decomposition techniques usually employed to study turbulent flows, such as SPOD and CS-SPOD, are not applicable. Instead, we use the most general form of space-time POD to study actuation transients. We demonstrate this approach on the transients of a plasma-controlled supersonic twin-rectangular jet, periodically forced in the SS symmetry component at $St = 0.9$. To help isolate the perturbations that arise due to the forcing from the background turbulence, we conduct synchronized simulations of the natural and forced jets, then perform space-time POD on a statistical ensemble of the perturbation quantities.

The space-time POD eigenvalues reveal low-rank behavior in the SS symmetry component, whose perturbation energy is well-captured by the leading mode. The remaining three symmetry components—SA, AS, and AA—exhibit slow rank decay. The SS and AS leading modes show that the initial pulse of the actuator has the greatest effect, generating a high-amplitude acoustic wave in the SS mode, and a wavepacket in the AS mode that briefly emerges before disappearing into turbulence. The SS mode highlights the mean flow deformation transient occurring near the nozzle

centerline, specifically, a reduction in shock spacing due to the forcing. No significant effect on screech is observed—a finding that is also supported by local frequency-time analysis of the forced jet.

Analysis of the instantaneous, spatially-integrated energy of the leading modes shows that all four D_2 symmetry components attain approximately 90% of their energy in the long-time limit within 50 time units after the actuation starts. This provides an energy-based estimate of the length of the actuation transient. At the conclusion of the transient, time-averaged statistics, including acoustic spectra and sound pressure levels, may be collected for episode-based machine learning control of jet noise.

Acknowledgments

We gratefully acknowledge support from Office of Naval Research award N00014-23-1-2457, under the supervision of Dr. Steve Martens. LES calculations were carried out on the "Onyx" Cray XC40/50 and "Carpenter" Cray EX4000 systems in ERDC DSRC, using allocations provided by DoD HPCMP.

References

[1] Brès, G. A., and Lele, S. K., "Modelling of jet noise: a perspective from large-eddy simulations," *Phil. Trans. R. Soc. A*, Vol. 377, No. 20190081, 2019, pp. 1–23. https://doi.org/https://doi.org/10.1098/rsta.2019.0081.

[2] Jordan, P., and Colonius, T., "Wave packets and turbulent jet noise," *Annu. Rev. Fluid Mech.*, Vol. 45, 2013, pp. 173–195. https://doi.org/https://doi.org/10.1146/annurev-fluid-011212-140756.

[3] Schmidt, O. T., Towne, A., Rigas, G., Colonius, T., and Brès, G. A., "Spectral analysis of jet turbulence," *J. Fluid Mech.*, Vol. 855, 2018, pp. 953–982. https://doi.org/https://doi.org/10.1017/jfm.2018.675.

[4] Samimy, M., Webb, N., Esfahani, A., and Leahy, R., "Perturbation-based active flow control in overexpanded to underexpanded supersonic rectangular twin jets," *J. Fluid Mech.*, Vol. 959, No. A13, 2023, pp. 1–34. https://doi.org/https://doi.org/10.1017/jfm.2023.139.

[5] Samimy, M., Adamovich, I., Webb, B., Kastner, J., Hileman, J., Keshav, S., and Palm, P., "Development and characterization of plasma actuators for high-speed jet control," *Exp. Fluids*, Vol. 37, 2004, pp. 577–588. https://doi.org/https://doi.org/10.1007/s00348-004-0854-7.

[6] Brès, G. A., Yeung, B. C. Y., Schmidt, O. T., Esfahani, A., Webb, N., Samimy, M., and Colonius, T., "Towards large-eddy simulations of supersonic jets from twin rectangular nozzle with plasma actuation," *AIAA paper 2021-2154*, 2021. https://doi.org/https://doi.org/10.2514/6.2021-2154.

[7] Yeung, B. C. Y., Schmidt, O. T., and Brès, G. A., "Three-Dimensional Spectral POD of Supersonic Twin-Rectangular Jet Flow," *AIAA paper 2022-3345*, 2022. https://doi.org/https://doi.org/10.2514/6.2022-3345.

[8] Yeung, B. C. Y., and Schmidt, O. T., "Plasma Actuation and Bispectral Mode Decomposition of Supersonic Twin-Rectangular Jet Flow," *AIAA paper 2023-4177*, 2023. https://doi.org/https://doi.org/10.2514/6.2023-4177.

[9] Schmidt, O. T., and Schmid, P. J., "A conditional space–time POD formalism for intermittent and rare events: example of acoustic bursts in turbulent jets," *J. Fluid Mech.*, Vol. 867, No. R2, 2019, pp. 1–12. https://doi.org/https://doi.org/10.1017/jfm.2019.200.

[10] Lumley, J. L., *Stochastic Tools in Turbulence*, Academic Press, New York, 1970.

[11] Frame, P., and Towne, A., "Space-time POD and the Hankel matrix," *PLoS ONE*, Vol. 18, No. 8, 2023, p. e0289637. https://doi.org/https://doi.org/10.1371/journal.pone.0289637.

[12] Glauser, M. N., Leib, S. J., and George, W. K., "Coherent Structures in the Axisymmetric Turbulent Jet Mixing Layer," *Turbul. Shear Flows*, Vol. 5, 1987, pp. 134–145. https://doi.org/https://doi.org/10.1007/978-3-642-71435-1_13.

[13] Picard, C., and Delville, J., "Pressure velocity coupling in a subsonic round jet," *Int. J. Heat Fluid Flow*, Vol. 21, No. 3, 2000, pp. 359–364. https://doi.org/https://doi.org/10.1016/S0142-727X(00)00021-7.

[14] Towne, A., Schmidt, O. T., and Colonius, T., "Spectral proper orthogonal decomposition and its relationship to dynamic mode decomposition and resolvent analysis," *J. Fluid Mech.*, Vol. 847, 2018, pp. 821–867. https://doi.org/https://doi.org/10.1017/jfm.2018.283.

[15] Schmidt, O. T., and Colonius, T., "Guide to spectral proper orthogonal decomposition," *AIAA J.*, Vol. 58, No. 3, 2020, pp. 1023–1033. https://doi.org/https://doi.org/10.2514/1.J058809.

[16] Heidt, L., and Colonius, T., "Spectral proper orthogonal decomposition of harmonically forced turbulent flows," *J. Fluid Mech.*, Vol. 985, No. A42, 2024, pp. 1–48. https://doi.org/https://doi.org/10.1017/jfm.2024.70.

[17] Nikitin, N., "On the rate of spatial predictability in near-wall turbulence," *J. Fluid Mech.*, Vol. 614, 2008, pp. 495–507. https://doi.org/https://doi.org/10.1017/S0022112008003741.

[18] Nikitin, N. V., "Disturbance Growth Rate in Turbulent Wall Flows," *Fluid Dyn.*, Vol. 44, No. 5, 2009, pp. 652–657. https://doi.org/https://doi.org/10.1134/S0015462809050032.

[19] Unnikrishnan, S., and Gaitonde, D. V., "A high-fidelity method to analyze perturbation evolution in turbulent flows," *J. Comput. Phys.*, Vol. 310, 2016, pp. 45–62. https://doi.org/https://doi.org/10.1016/j.jcp.2016.01.017.

[20] Adler, M. C., and Gaitonde, D. V., "Dynamic linear response of a shock/turbulent-boundary-layer interaction using constrained perturbations," *J. Fluid Mech.*, Vol. 840, 2018, pp. 291–341. https://doi.org/https://doi.org/10.1017/jfm.2018.70.

[21] Nikitin, N. V., and Pivovarov, D. E., "Perturbation Growth Rate in Turbulent Couette Flow," *Fluid Dyn.*, Vol. 53, No. 6, 2018, pp. 723–728. https://doi.org/https://doi.org/10.1134/S0015462818060204.

[22] Sirovich, L., "Turbulence and the Dynamics of Coherent Structures Part I: Coherent Structures," *Q. Appl. Maths*, Vol. 45, No. 3, 1987, pp. 561–571. https://doi.org/https://doi.org/10.1090/qam/910462.

[23] Brès, G. A., Ham, F. E., Nichols, J. W., and Lele, S. K., "Unstructured Large-Eddy Simulations of Supersonic Jets," *AIAA J.*, Vol. 55, No. 4, 2017, pp. 1164–1184. https://doi.org/https://doi.org/10.2514/1.J055084.

[24] Brès, G. A., Bose, S. T., Ivey, C. B., Emory, M., and Ham, F., "GPU-accelerated large-eddy simulations of supersonic jets from twin rectangular nozzle," *AIAA paper 2022-3001*, 2022. https://doi.org/https://doi.org/10.2514/6.2022-3001.

[25] Chu, B.-T., "On the Energy Transfer to Small Disturbances in Fluid Flow (Part I)," *Acta Mech.*, Vol. 1, 1965, pp. 215–234. https://doi.org/https://doi.org/10.1007/BF01387235.

[26] Sirovich, L., and Park, H., "Turbulent thermal convection in a finite domain: Part I. Theory," *Phys. Fluids*, Vol. 2, No. 9, 1990, pp. 1649–1658. https://doi.org/https://doi.org/10.1063/1.857572.

[27] Kim, J., Afshari, A., Bodony, D. J., and Freund, J. B., "LES Investigation of a Mach 1.3 Jet With and Without Plasma Actuators," *AIAA paper 2009-290*, 2009. https://doi.org/https://doi.org/10.2514/6.2009-290.

[28] Edgington-Mitchell, D., Li, X., Liu, N., He, F., Wong, T. Y., Mackenzie, J., and Nogueira, P., "A unifying theory of jet screech," *J. Fluid Mech.*, Vol. 945, No. A8, 2022, pp. 1–24. https://doi.org/https://doi.org/10.1017/jfm.2022.549.